HYPERSONIC FLOW FIELDS AROUND HERMES COMPUTED BY EULER CODES

B. Arlinger * and B. Winzell **
Saab Aircraft Division
Linköping, Sweden

Abstract

The flow field around a complete Hermes configuration has been computed by combining a time–marching and a space–marching Euler code. The computations have been done for hypersonic Mach numbers and high angles of attack with special focus on the leeside flow patterns. The combination of time– and space–marching technique for the Euler equations is very cost–effective, because the time–marching solver, which is the most time–consuming, is applied only in the nose region where a subsonic pocket exists.

Results are presented for grids with more than 10 million points, and a comparison is also made between a coarse grid time–marching solution around a larger part of Hermes and a space–marching solution.

I Introduction

In the process of designing the European space shuttle Hermes a large amount of computational work is done to investigate the flow field and especially the pressure and heat flux loads on the configuration during the reentry phase. Because of the difficulties to simulate the reentry aerothermodynamics experimentally, there is a great need for efficient computational tools. These should include codes of various types: Euler, boundary layer and Navier Stokes codes with different levels of high temperature gas dynamics including chemical nonequilibrium.

In the present work only the inviscid problem is studied, i e the Euler equations are solved. This is a logical step before going to the Navier Stokes equations. The Euler codes applied have previously been used in transonic and supersonic cases and for geometries quite different from the Hermes shape. The time–marching code uses an explicit multistep scheme in finite volume formulation based on Jameson's FLO57 [1]. Also in the space–marching code an explicit finite volume scheme is applied [2].

Ref 1 gives a good overview of the most used time–marching Euler solvers of explicit type, and further references. A number of space–marching Euler solvers are reviewed in Ref 3, with an emphasis on their application to flow around missiles.

One reason for choosing explicit flow solvers is the easiness with which they can be applied to different grid topologies. Thus, for the Hermes geometry varying grid types had to be used to get good grid resolution, especially around the Hermes leeside.

Features of interest to investigate in applications to hypersonic flow cases are the shock capturing approach, suitable forms and levels of the artificial viscosity terms, stability and convergence properties, etc.

For the high angles of attack that are of interest here the leeside flow is expected to be quite complex, containing vortices, cross flow shock waves, etc. The effects on this flow field of neglecting the physical viscosity will be clarified in subsequent computations based on Navier Stokes equations. An interesting comparison between the Euler and Navier Stokes approach for a slightly earlier Hermes geometry version has already been done, with preliminary results shown in Ref 4.

In the present computations perfect gas relations are used throughout, although the results for M = 10 should be influenced by vibrational excitation effects.

II Mathematical Formulation

The Euler equations expressing conservation of mass, momentum and energy may be written

$$\frac{\partial \rho}{\partial t} + \mathrm{div}\,(\rho \mathbf{V}) = 0 \qquad (1a)$$

$$\frac{\partial (\rho \mathbf{V})}{\partial t} + \mathrm{div}\,(\rho \mathbf{V}\mathbf{V} + p\mathbf{I}) = 0 \qquad (1b)$$

$$\frac{\partial e}{\partial t} + \mathrm{div}\,(\rho \mathbf{V} H) = 0 \qquad (1c)$$

where ρ, p and t denote density, pressure and time, V is the velocity vector, e is the total energy per volume and H the total enthalpy defined by

$$e = \frac{p}{\gamma - 1} + \rho \frac{V^2}{2} \qquad (2)$$

$$H = \frac{e + p}{\rho} \qquad (3)$$

* Head, Computational Aerodynamics

** Research Scientist, Flutter and Loads

The time–dependent Eqs (1) have to be used whenever the flow contains subsonic regions, in which case the numerical scheme is marched in time until steady state is achieved with sufficient accuracy. In contrast to this procedure, which requires a great number of updatings of the whole flow field, a much more efficient solution algorithm can be used in purely supersonic flow. This is based on the fact that for supersonic flow the equations are hyperbolic in space. The steady version of the equations is then used to obtain the solution in a single downstream space–marching sweep.

The approach taken in the present work, is to apply the time–dependent solver only where it is needed, i e in the nose region of Hermes, where a subsonic pocket exists for all free stream Mach numbers. The downstream boundary for these calculations is chosen at a plane normal to the flow, located in purely supersonic flow, where boundary conditions of extrapolation type are applied. After the solution has converged, the downstream boundary plane becomes the initial field for a single space–marching sweep over the remaining purely supersonic field around Hermes.

III The Time–Marching Euler Code

Flow Solver

The time marching flow solver is essentially the finite volume FLO57 method by A Jameson. Its characteristics are well known and described in detail, for instance in Ref 1. The fundamental ingredients in the solver are the use of multi–stage time integration of the descritized (in space) Eqns (1), the use of local time steps to advance the overall approximate solutions towards steady state as quickly as possible, the combination of a second order shock capturing artificial dissipation and a forth order backgrund filtering to prevent oscillatory errors. The code has also a residual smoothing option, which usually further accelerates the convergence.

The Saab version of the code has several extended features, as block structured grid handling with a versatile block interface and boundary condition treatment. In order to tune the method for hypersonic computations on grids of the polar type structure to be described below, the use of dummy cells to accurately monitor the boundary and interface conditions was further elaborated to achieve robust computations. Similarly, the end conditions for artificial dissipation and residual smoothing had to be improved.

Prior to the Hermes computations the shock capturing ability of the code was demonstrated in order to ensure correct shock stand off distance on spherical bodies in high supersonic flow and in order to demonstrate robust convergence.

Computational Grid

The blunt shape of the Hermes nose motivates a C–O type grid for the forebody calculation. A special grid generation program was written, using as input the intersection curves of the vehicle with vertical planes.

The resulting grid is characterized by a singular line from the nose in the upstream direction. All streamwise coordinate lines emanate from this singular axis. The downstream boundary on the other hand, is placed aft enough to guarantee purely supersonic velocities, and this boundary is part of a plane, orthogonal to the principal axis of the space craft. This is where all the streamwise coordinate lines end.

In between, the mesh is built from 2–D surfaces, which in the early nose region are bent forward. The detailed subdivision of these surfaces into quadrilaterals is guided by first a sequence of conformal mappings to render the transformed body curve a more convex shape. Then we construct a field of normals to the boundary, which is smoothed and then used as germs for outgoing coordinate lines. The outgoing coordinate curves end at a limiting far field surface, consisting of a cone and a sperical cap.

Before carrying out the inverse transformation a few smoothing sweeps are taken. See Fig 1 for the general features of the resulting grid.

IV The Space–Marching Euler Code

Flow Solver

The time–independent version of Eqs. 1 can be written

$$\frac{\partial E}{\partial x} + \frac{\partial F}{\partial y} + \frac{\partial G}{\partial z} = 0 \qquad (4)$$

with E, F and G defined as

$$E = \begin{pmatrix} \rho u \\ \rho u^2+p \\ \rho uv \\ \rho uw \end{pmatrix} \quad F = \begin{pmatrix} \rho v \\ \rho vu \\ \rho v^2+p \\ \rho vw \end{pmatrix} \quad G = \begin{pmatrix} \rho w \\ \rho wu \\ \rho wv \\ \rho w^2+p \end{pmatrix} \qquad (5)$$

The energy equation is here reduced to H = constant.

The solver is essentially the same as in the program SUMA[2] developed for supersonic marching computations at Saab. The equations are discretized on a grid around Hermes based on planes cutting the space shuttle normal to its length direction. An explicit marching operator of MacCormack type is used to advance the solution from one plane to the next. Because of the explicit formulation a stability condition has to be satisfied, which determines the marching step length from plane to plane. After the step to the next plane is computed, the 2D grid is automatically generated in that plane.

The marching algorithm is written in fully conservative form in a finite volume formulation. The shocks are captured as in the time–dependent approach, but because they always are

weak in a purely supersonic field, they do not create a problem even for high hypersonic free stream cases.

Artificial viscosity terms are used to damp numerically generated oscillations. With the finite volume marching scheme formally written as

$$E_{i+1}\,\Delta S_{i+1} = E_i\,\Delta S_i - \sum_k (E, F, G)\cdot \Delta S_k + D$$

the artificial viscosity is denoted by D. ΔS_i stands for the cell end face in the constant x plane with index i, and the summation is made over the four cell side faces with the area vector ΔS_k. The viscosity term D, evaluated at station i, is of a type analogous to that used in the time–marching code. The algorithms used are

$$D = \frac{\Delta x\,(\Delta y + \Delta z)}{2}\left(d_{j+\frac{1}{2},k} - d_{j-\frac{1}{2},k} + d_{j,k+\frac{1}{2}} - d_{j,k-\frac{1}{2}} \right)$$

$$d_{j+\frac{1}{2},k} = \varepsilon^{(2)}_{j+\frac{1}{2},k}\left(E_{j+1,k} - E_{j,k} \right) - \varepsilon^{(4)}_{j+\frac{1}{2},k}\left(E_{j+2,k} - 3E_{j+1,k} + 3E_{j,k} - E_{j-1,k} \right)$$

$$\varepsilon^{(2)}_{j+\frac{1}{2},k} = c_2 \max\left(\nu_{j+1,k}, \nu_{j,k} \right)$$

$$\varepsilon^{(4)}_{j+\frac{1}{2},k} = \max\left(0, c_4 - \varepsilon^{(2)}_{j+\frac{1}{2},k} \right)$$

$$\nu_{j,k} = \frac{\left| p_{j+1,k} - 2p_{j,k} + p_{j-1,k} \right|}{p_{j+1,k} + 2p_{j,k} + p_{j-1,k}}$$

with corresponding expressions for $d_{j,k+1/2}$. Δx is the marching step and Δy and Δz are constants for the whole field related to the cell dimensions in transversal direction. The constants c_2 and c_4 are prescribed and control the artificial viscosity level.

Computational Grid

A 2D grid is automatically generated in each new cross section plane through Hermes as the marching goes on. Two types of grid can be generated in these planes: body type and body–wing type grids, see Fig 2. Both tend to a Cartesian, or skewed Cartesian, type grid in the far field. The body–wing type grid was chosen to avoid a singular point at the upper wing body cross section and to have good resolution at the wing leading edge.

The grid varies smoothly from plane to plane, except at a number of prescibed x stations where jumps in grid type or number of grid cells are permitted. At these stations the solution variables are interpolated from the previous grid to the next, before the marching proceeds. Typically 4 to 5 such stations were used in the Hermes computations in order to get a good resolution along the whole configuration.

The cross section grids are generated by algebraic technique. For the body type grids transfinite interpolation is used, but for the body–wing type grid a more geometrically oriented method had to be used to get good results.

Both generators start by computing a suitable grid point distribution along the centerline and body contours. The point spacing on the body is essentially controlled by a given minimum cell width, so the number of cells on the body varies as the perimeter does. For the body–wing type grid the number of points on the wing upper and lower surface is a prescribed constant, that is set in each of the intervals between the grid jump stations. The distribution of these wing surface points is controlled by an exponential expression.

Next, an approximately horizontal and two vertical grid lines are generated for the body–wing type grid, all leaving the wing leading edge point, see Fig 3. These lines are changing smoothly from plane to plane and their slopes at the leading edge are controlled to give a good H type grid there. The grid points along these curves and the grid outer boundaries are computed, taking into account the denser point distribution close to the leading edge. The grids are then generated in the four areas defined by the three curves and the Hermes contour. The generation starts from the horizontal contours and proceeds up– or downwards by adding proper normal distances to the horizontal type contours. A couple of smoothing sweeps over the complete grid ends the generation.

V Computational Results

Time– and Space–marching Comparison

To validate the coupling between the two Euler solvers and to compare results on different grids, a time–marching solution was computed for a major portion of Hermes 94, a pre–version to Hermes 0.0, and then a coupled solution was computed. The flow case chosen was M = 7 and α = 15 °. A grid containing 81x33x65 points was used for the time–marching cases, while the space–marching grid in the cross section planes had almost 5 times as many points, and also was much denser in the streamwise direction.

A general view of the grid and results in the symmetry plane from the time–marching solution over the major Hermes portion is seen in Fig 4. In the coupled solution the space–marching procedure was started in the canopy region and proceeded to the end of the configuration. To compare results from the two solvers, Fig 5 shows grids and Mach number distributions in a cross section near the start of the winglets. Although the grid topologies and densities are seen to differ clearly between the time– and space–marching solutions, the Mach contours are quite similar. The bow shocks are sensitive to both grid resolution and smoothness.

Coupled Solutions

The configuration studied was Hermes 0.0, for which coup-

led time– and space–marching solutions were computed at M = 6.4, α = 30 °, M = 10.0, α = 15 ° and M = 10.0, α = 30 °.

The time–marching solutions were computed over the first 3.3 meters of Hermes, to include also the canopy shock waves in those solutions, and then the space–marching solutions were computed for 9.2 meters up to the end of the configuration. The grid for the first part contained 81x33x65 points in the spanwise, normal and circumferential directions (only one side of the symmetric configuration computed). In the space–marching part the grids had 85x176 points per plane. The number of marching planes varied between 550 and 865 depending on the case, because of the stability requirements of the explicit marching operator.

A number of results with combined grids and Mach contours are presented next for the M = 6.4 case. In Fig 6 a perspective view is shown of the nose portion, and in Fig 7 a cross section result is illustrated at the x station 5.0 meters (nose point is at 2.5 m), still within the time–marching solution region. The figures show a well resolved bow and canopy shock. The space–marching results in Fig 8 a – c illustrate a few cross section grids and Mach contour patterns. Besides the bow shock, two other Mach number discontinuities are seen: one starting on the wing close to the body side, moving outwards and up on the winglet, and the other a cross flow shock wave on the upper part of the fuselage. The lower and oblique part of the first discontinuity seems, at the last station, to be a contact discontinuity rather than a shock wave. At the earlier stations, however, this part is a cross flow normal discontinuity, i e a shock wave.

The sensitivity of shock waves to local grid types is illustrated by comparing the bow shocks in Figs 7 and 8a. Effects on the shape and crispness of the shock wave are seen both due to grid resolution, alignment and skewness.

Computed Mach contours for the two cases at M = 10 are given in Figs 9 to 12. The grids were the same as in the previous case, except for variations in the marching step size. A strong effect of the angle of attack is seen in the cross flow patterns. For the lower α the bow shock comes closer to the winglets, and the cross flow discontinuities are weaker, as would be expected. Thus, the fuselage shock wave does not appear in the flow at α = 15 °, and the wing cross flow shock wave is seen to be weaker and moves out only to half of the wing span.

In Fig 13 the cross flow velocities are shown in the last section for M = 10 and α = 30°. Two vortices are seen, one on top of the fuselage, inboard of the body cross flow shock wave, and the other above the wing, below the contact discontinuity. Also, the extensions of the cross flow shock waves can be recognized, as discussed above.

Recently performed calculations using Navier Stokes equations (not published yet) also show the vortices mentioned above, although their form and location is slightly different. In Ref 4 both Euler and Navier Stokes results are shown for an early Hermes geometry, illustrating the differences in form and extension of vortices and discontinuities.

A good overview of the surface Mach number pattern over the whole upper side of Hermes is provided by Figs 14 and 15. A slight disturbance in the contour pattern at the coupling section between time– and space–marching solution could be due to local grid type differences.

A comparison between the computed Mach contours for cases with different Mach number but the same α shows a high degree of similarity, illustrating the Mach number independence principle in hypersonic flow. This can be seen, for instance, from Figs 8c and 12c for α = 30 ° and M = 6.4 and 10 respectively.

To illustrate the computed flow characteristics in the leeside flow region, Mach contours are preferred instead of pressures. This is due to the very low pressure levels on the leeside compared to the dynamic pressure, which normally makes C_p contour plots void of any information there. As an example of this and of a situation with some noticeable pressure disturbance unrelated to the bow shock, Figs 16 and 17 show pressure contours and Mach contours for a section through the rising winglets. For the lower α case, the winglet leading edge has a sufficiently low sweep angle to cause an embedded shock wave around it, which gives a local pressure rise of significance.

The required computer times are of the order of 2 hours on a CRAY–1 for the time–marching part, and 1 to 2 hours on a VAX 8700 for the space–marching Euler solution.

VI Concluding Remarks

Combined time– and space–marching solutions of the Euler equations are presented for the European space shuttle project Hermes in hypersonic flow and at large angles of attack. Using the space–marching approach for the large supersonic part of the flow field is very cost–effective, and detailed flow field results are presented for grids with more than 10 million cells.

The Euler codes are written in a finite volume, shock capturing form with artificial viscosity terms of the Jameson type. The grid in the space–marching part was abruptly changed at a number of x stations to keep a good resolution above the whole wing.

A logical continuation of the present work is to do Navier Stokes computions on the Hermes geometry. Wether a space marching approach, i e a PNS solution, can be made to give correct results for a high incidence case, is, however, doubtful. Results so far with a global time–marching approach for the Navier Stokes equations indicate the large differences in computer time required in comparison to the work presented here.

VII References

1. Jameson, A., "Successes and Challenges in Computational Aerodynamics", AIAA Paper 87–0602.

2. Arlinger, B., "Computation of Supersonic Flow about Complex Configurations", ICAS Paper 84–1.3.2.

3. Priolo, F. J. and Wardlaw, A. B., "A Comparison of Inviscid Computational Methods for Supersonic Tactical Missiles", AIAA Paper 87–0113.

4. Rieger, H. and Jameson, A., "Solution of Steady Three–Dimensional Compressible Euler and Navier–Stokes Equations by an Implicit LU Scheme", AIAA Paper 88–0619.

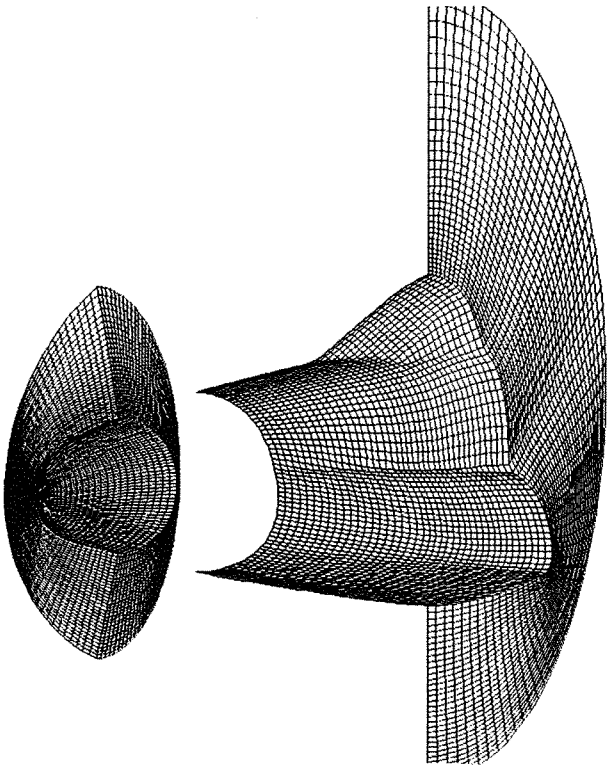

Fig 1. Grid around Hermes nose for time–marching solution

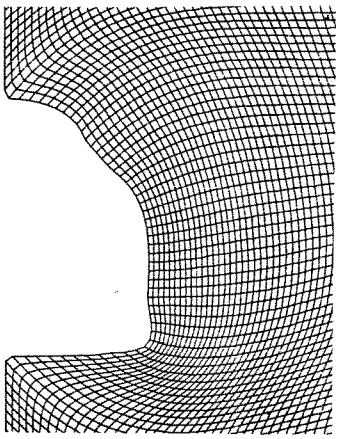

a) Body type grid

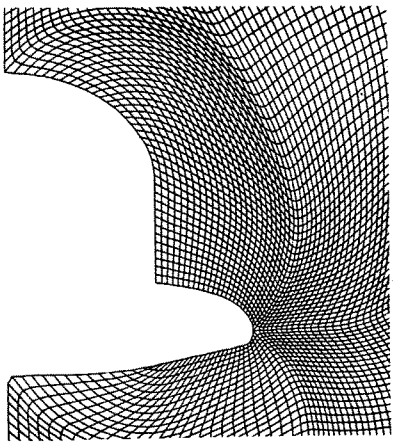

b) Body–wing type grid

Fig 2. Cross section grid types for space marching solution

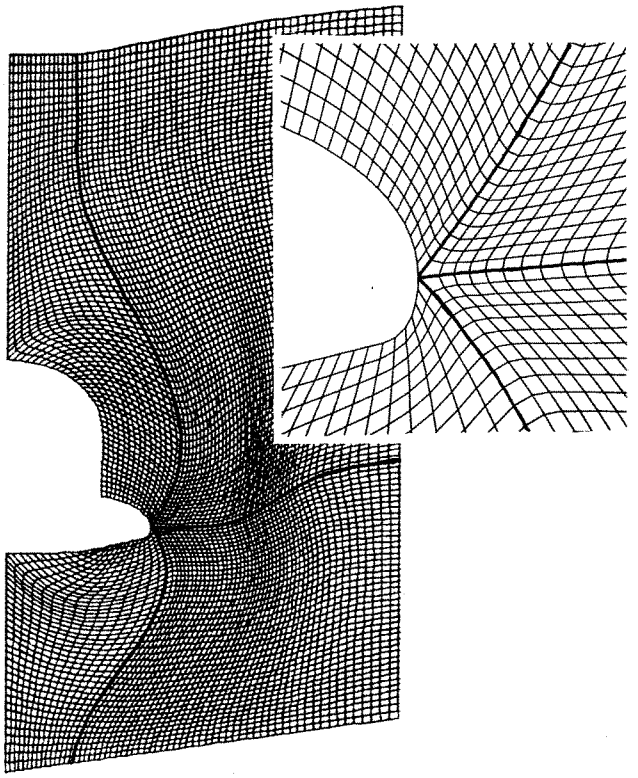

Fig 3. Subdivision used in generation of body–wing type grids

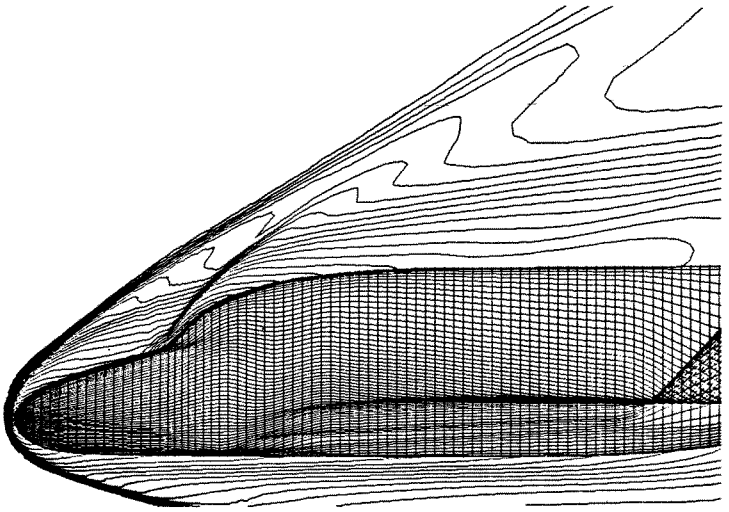

Fig 4. Global time–marching Euler computation around Hermes 94 at M = 7 and $\alpha = 15°$. Surface grid and Mach contours in symmetry plane. $\Delta M = 0.25$.

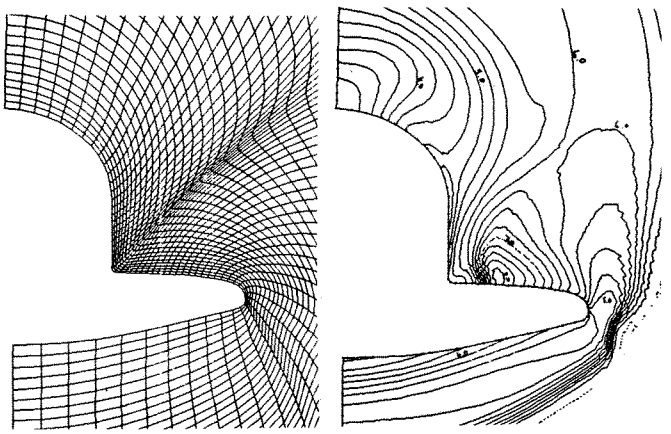

a) Time–marching Euler solution

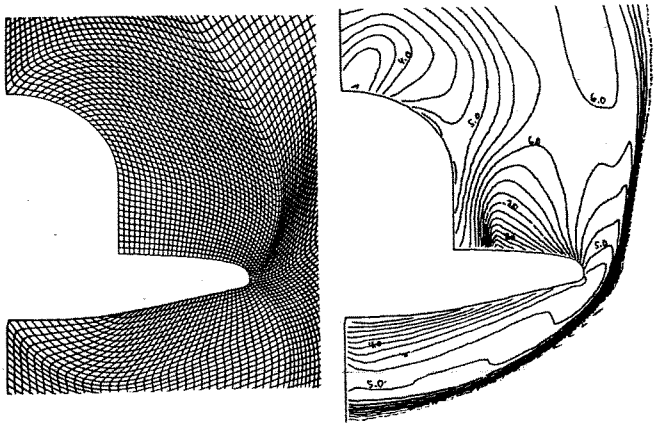

b) Space–marching Euler solution

Fig 5. Grids and Mach contours at x = 11 m on Hermes 94 at M = 7 and $\alpha = 15°$. $\Delta M = 0.25$.

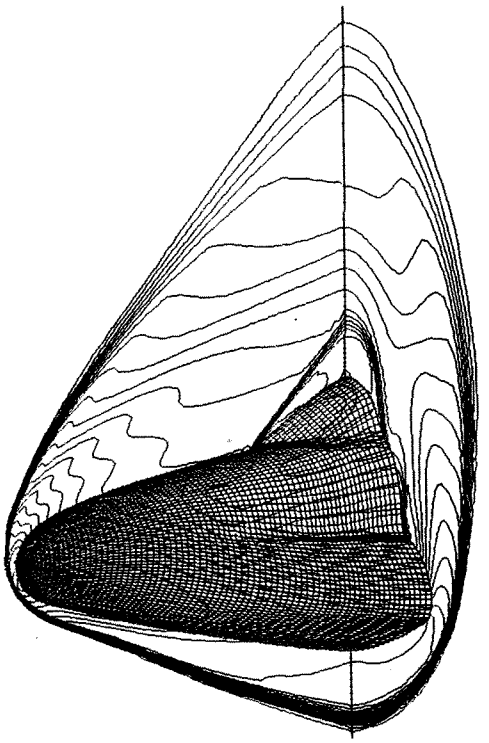

Fig 6. Mach contours on Hermes 0.0 forebody at M = 6.4 and $\alpha = 30°$. Time–marching Euler solution. $\Delta M = 0.25$.

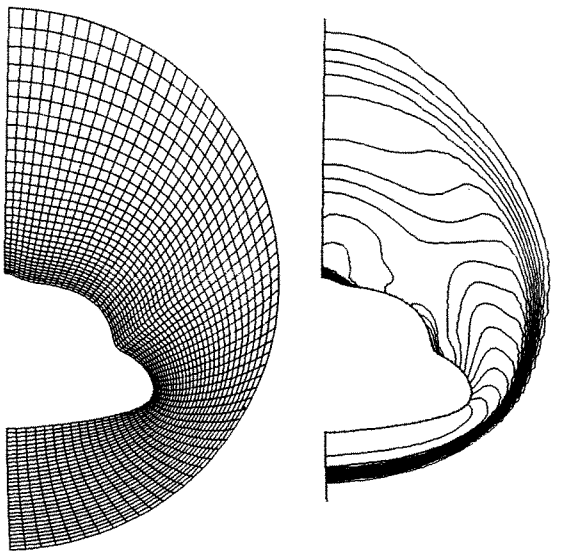

Fig 7. Grid and Mach contours at section x = 5 m for Hermes 0.0 at M = 6.4 and $\alpha = 30°$. Time–marching Euler solution. $\Delta M = 0.25$.

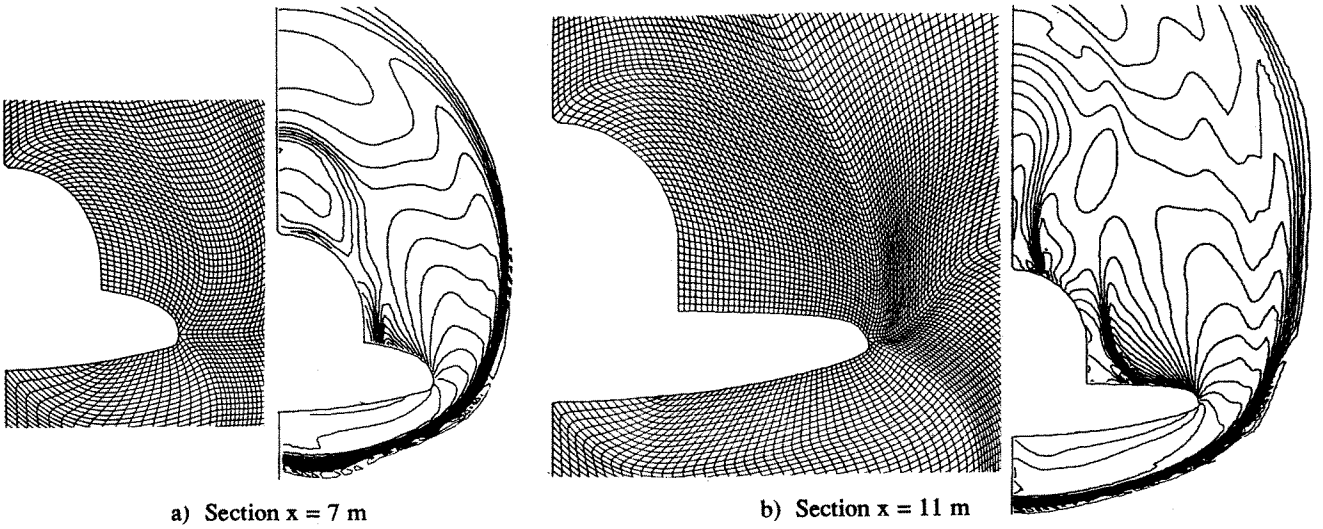

a) Section x = 7 m

b) Section x = 11 m

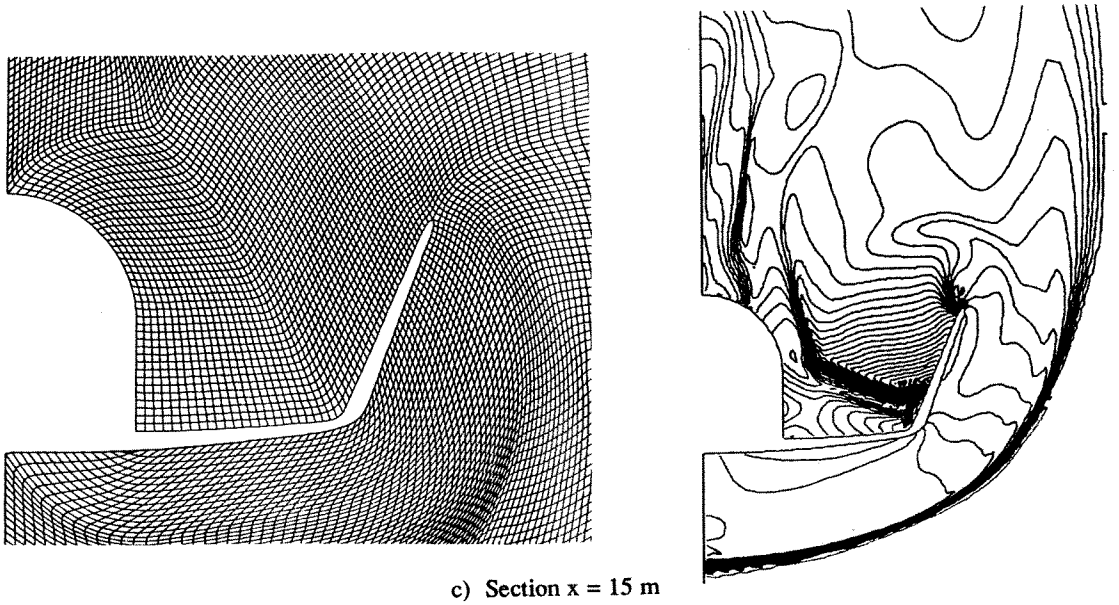

c) Section x = 15 m

Fig 8. Grids and Mach contours at sections through Hermes 0.0 at M = 6.4 and $\alpha = 30°$. Space–marching Euler solution. $\Delta M = 0.25$.

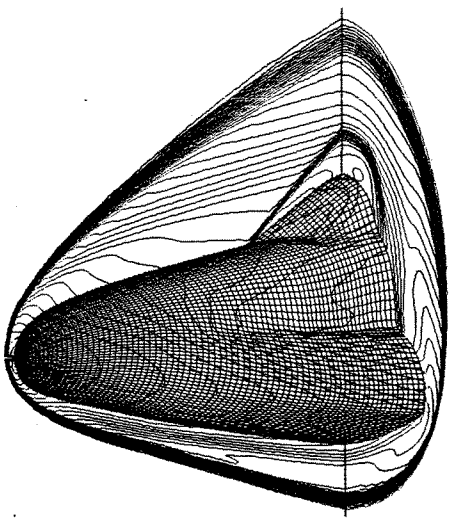

Fig 9. Mach contours on Hermes 0.0 forebody at M = 10 and $\alpha = 15°$. Time–marching Euler solution. $\Delta M = 0.25$.

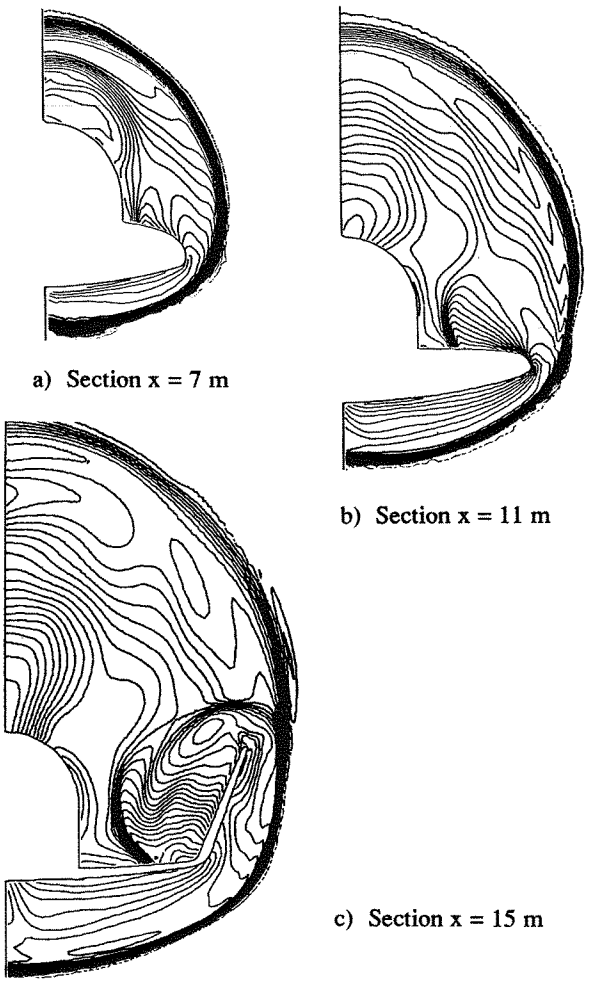

Fig 10. Mach contours at sections through Hermes 0.0 at M = 10 and $\alpha = 15°$. Space–marching Euler solution. $\Delta M = 0.25$.

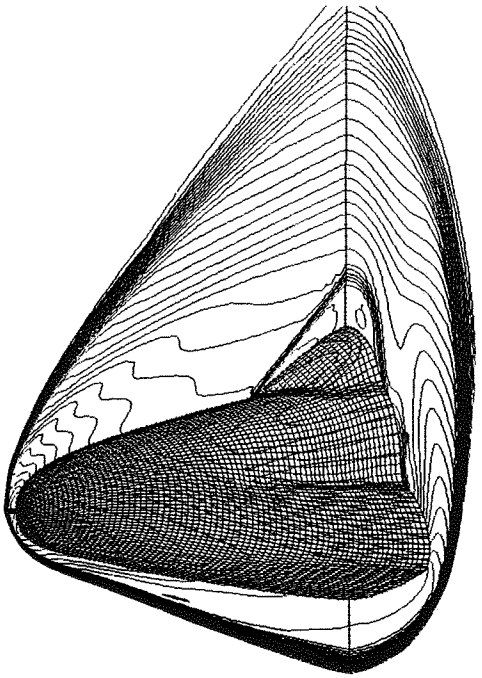

Fig 11. Mach contours on Hermes 0.0 forebody at M = 10 and $\alpha = 30°$. Time–marching Euler solution. $\Delta M = 0.25$.

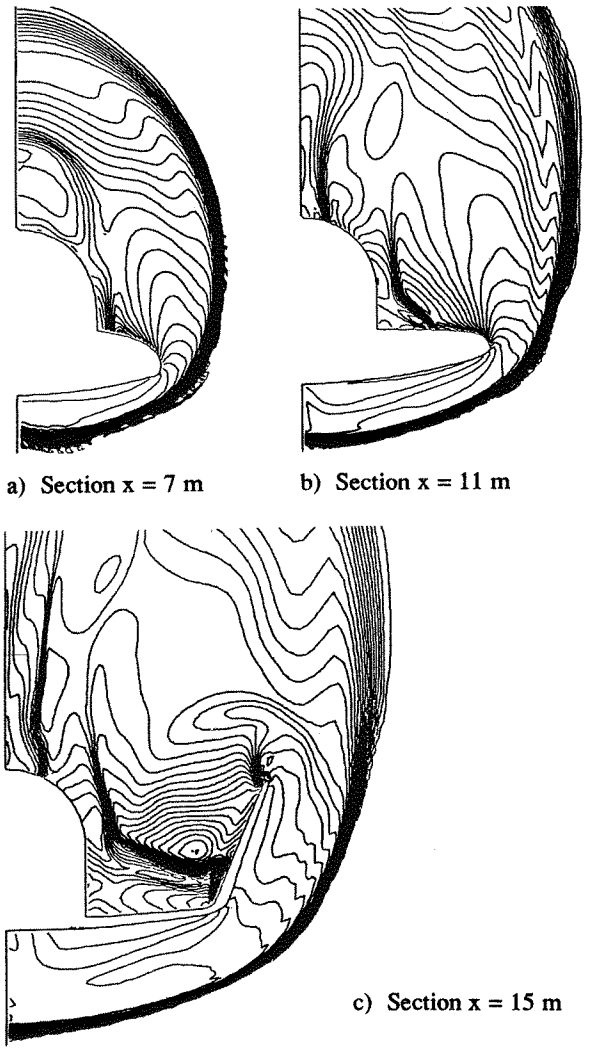

Fig 12. Mach contours at sections through Hermes 0.0 at M = 10 and $\alpha = 30°$. Space–marching Euler solution. $\Delta M = 0.25$.

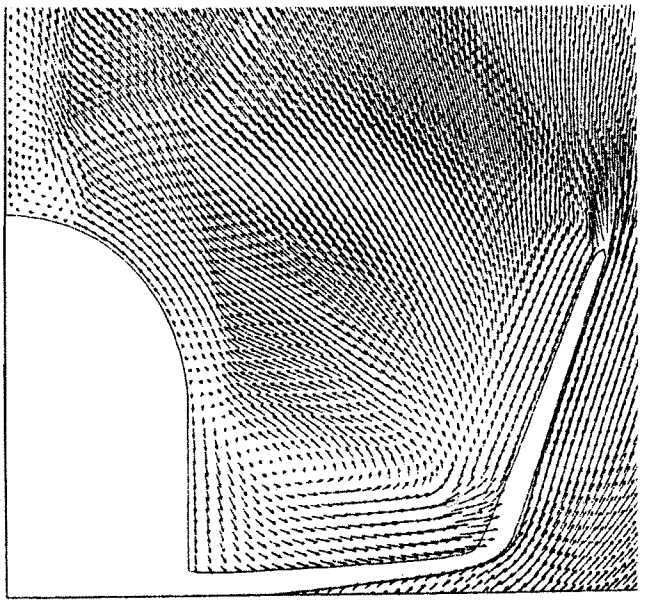

Fig 13. Cross flow velocities in section x = 15 m for M = 10 and $\alpha = 30°$.

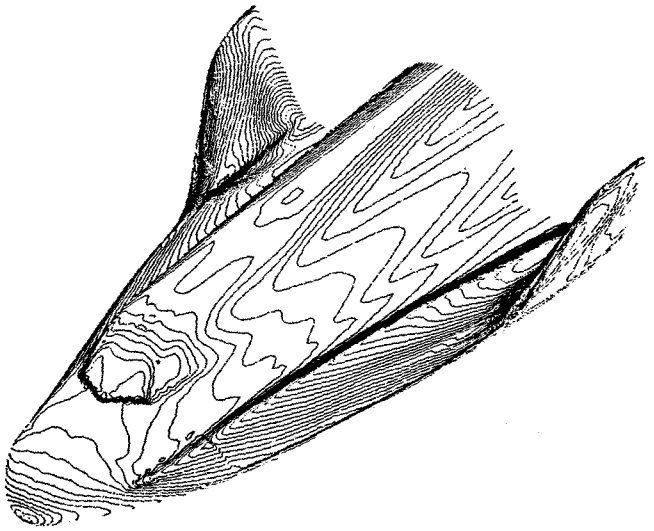

Fig 14. Surface Mach contours on Hermes 0.0 at M = 10 and α = 15°. $\Delta M = 0.25$.

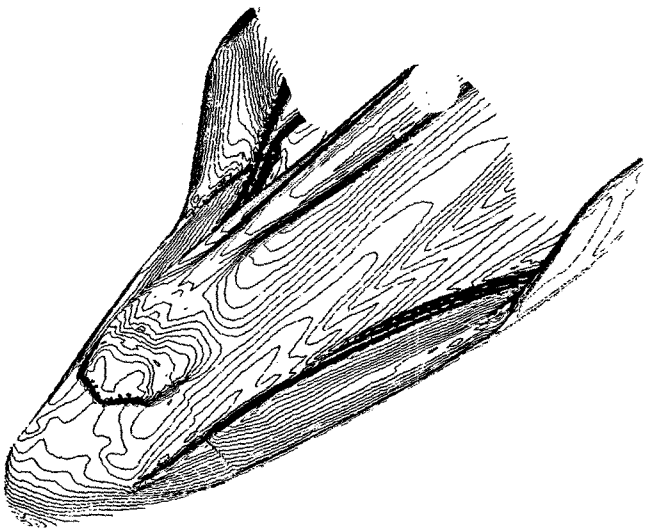

Fig 15. Surface Mach contours on Hermes 0.0 at M = 10 and α = 30°. $\Delta M = 0.25$.

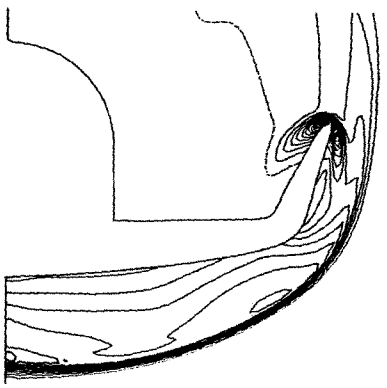

a) Pressure contours, $\Delta C_p = 0.02$

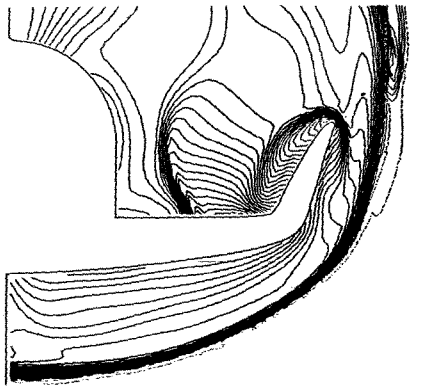

b) Mach contours, $\Delta M = 0.25$

Fig 16. Pressure and Mach contours in section x = 13 m for M = 10 and α = 15°.

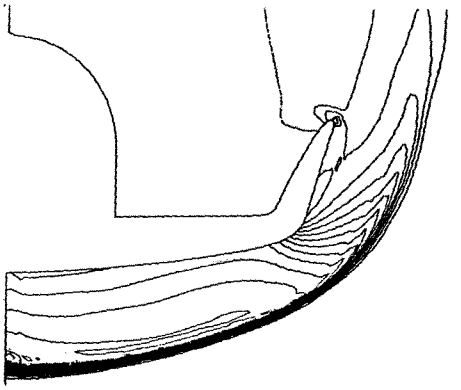

a) Pressure contours, $\Delta C_p = 0.02$

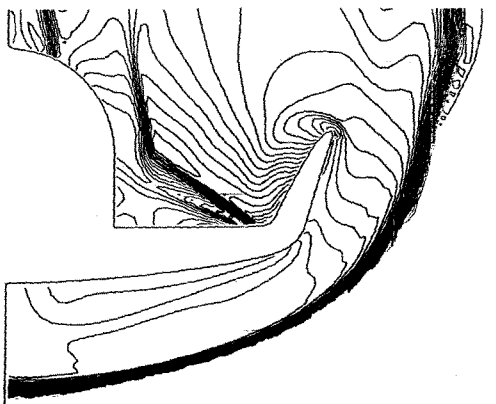

b) Mach contours, $\Delta M = 0.25$

Fig 17. Pressure and Mach contours in section x = 13 m for M = 10 and α = 30°.